Multiple-homojunction gradient nitrogen doped TiO2 for photocatalytic degradation of sulfamethoxazole, degradation mechanism, and toxicity assessment

Amir Mirzaei, Mustapha Eddah, Stéphanie Roualdès, Dongling Ma, Mohamed Chaker

Multiple-homojunction gradient nitrogen doped TiO_2 for photocatalytic degradation of sulfamethoxazole, degradation mechanism, and toxicity assessment

Amir Mirzaei [a,*], Mustapha Eddah [a,b], Stéphanie Roualdes [b], Dongling Ma [a], Mohamed Chaker [a,*]

[a] *Institut National de la Recherche Scientifique, Centre Énergie, Matériaux et Télécommunications, 1650 Boul. Lionel-Boulet, Varennes, Québec J3X 1S2, Canada*
[b] *Institut Européen des Membranes (IEM), UMR-5635, Univ Montpellier, ENSCM, CNRS, Place Eugène Bataillon, 34095 Montpellier, France*

Abstract

In this work, by using pulsed laser deposition (PLD) method, we incorporated nitrogen into the anatase TiO_2 lattice to fabricate substitutional nitrogen doped TiO_2 with different N content and film densities. All synthesized films were characterized in depth by X-ray diffraction (XRD), X-ray reflectivity (XRR), X-ray photoelectron spectroscopy (XPS), scanning electron microscopy (SEM), atomic force microscopy (AFM) and UV–vis spectroscopy. In the next step, to fully leverage the band bending induced by nitrogen doping, we synthesized a six layer multiple-homojunction using gradient nitrogen doped TiO_2 (g-N-TiO_2) to extend the width of band bending over the bulk of the porous photocatalyst and induce an oriented electrical field perpendicular to the substrate. Following its higher photoelectrochemical (PEC) performance, the multiple-homojunction g-N-TiO_2 prepared at 20 Pa with columnar-like nanostructure was used for the photocatalytic degradation of sulfamethoxazole (SMX) antibiotic in water under the simulated solar light irradiation. The results showed that compared to pristine TiO_2 and non-gradient doped TiO_2 (N-TiO_2), the photocatalytic degradation performance of g-N-TiO_2 dramatically improved in terms of SMX removal percentage, kinetics of degradation (10 times higher than TiO_2) and detoxification of solution. We believe that the superior potential of the PLD technique in controlling the film density and gradient doping renders it a highly promising technique towards fabricating unique multiple-homojunctions based on gradient doped semiconductors. Besides water treatment, such formed, precisely controlled, multiple-homojunctions with low interfacial defects will provide novel insights into other applications such as solar fuels, sensors, water splitting, solar cells, etc.

Keywords: gradient doping; N-doped TiO_2; pulsed laser deposition; water treatment; homojunction

* Corresponding authors.

E-mail: chaker@emt.inrs.ca (M. Chaker); amir.mirzaei@inrs.ca (A. Mirzaei)

1. Introduction

The presence of antibiotics such as sulfamethoxazole (SMX) in aquatic environment is considered as a rising environmental concern due to their adverse effects on ecosystems and on the development of antibiotic resistant bacteria [1]. Sulfamethoxazole is a widely prescribed antibiotic in both human and veterinary medicine to treat infectious diseases [2]. Due to its high consumption and high excretion rate, SMX is frequently detected in the aquatic environment such as surface water and underground aquifers, soil and even drinking water [3]. Accordingly, SMX is listed among the most frequently detected compounds in groundwater by U.S. Geological Survey [4] and it is usually considered as an antibiotic pollution indicator in environment [5]. Regarding its antibacterial nature and recalcitrant properties, SMX removal efficiency in conventional biological water treatment systems is low (< 30%) [2, 6].

Photocatalytic degradation of organic contaminants is a promising process based on the formation of electron and hole pairs under light irradiation with photon energy equal to or higher than the band gap of semiconducting materials [7]. Among various semiconducting materials, TiO_2 has attracted unprecedented interest due to its high photocatalytic activity, high stability and non-toxicity [8]. However, the relatively large band gap of TiO_2 (3.0-3.2 eV) limits its applications to the ultraviolet (UV) light region, which however represents only ∼4% of sunlight energy [9]. In addition, rapid recombination of charge carriers severely restricts the photocatalytic activity of semiconducting materials in general [10]. Notably, a low removal efficiency of the photocatalysis degradation process may lead to the formation of intermediates and by-products, which might be more toxic than their parent compounds [1, 11, 12]. Therefore, developing a highly efficient treatment process is needed to degrade recalcitrant contaminants such as antibiotics in aquatic media.

It is proven that the formation of multi-homojunction with gradient-doped concentration can simultaneously enhance light absorption and charge separation through the generation of an extended band bending and an oriented electric field [13-15]. In gradient-doped homojunctions, the extension of band bending can be tuned by gradually changing the dopant concentration [16]. Moreover, compared to the heterojunction structure, the lattice mismatch, defects and impurities at the interface can be significantly reduced in the homojunction [13, 17-19]. Notably, not only the dopant concentration but also its location (substitutional or interstitial) can significantly affect the photocatalytic performance [20]. However, the precise control of dopant concentration and position in the lattice and the fabrication of homojunctions with high quality interfacial contact between layers remain a challenge in terms of synthesis. Liu et al. [21] synthesized gradient vanadium doped TiO_2 by layer-by-layer sol-gel method for dye-sensitized solar cell application. Nevertheless, the fabrication of homojunctions with a precise and controlled concentration of dopant and a high quality interfacial attachment between layers by using wet chemical methods is tedious. Wang et al. [10] employed ion implantation to introduce nitrogen into a ZnO nanorod structure to form gradient N-doped ZnO structure. Although ion implementation can naturally introduce gradient doping into the host structure, the penetration depth of ions is limited. Abdi et al. [13] significantly improved water splitting efficiency by using gradient W doped $BiVO_4$ prepared by spray pyrolysis.

Although using gradient doping to enhance charge carrier separation is a well-established concept, most of the experimental works in this subject have employed wet chemical methods for photocatalysts preparation. While chemical methods are easy to implement and cost-effective, the chemically prepared films generally suffer from the inherent presence of residual precursors, reproducibility problems and difficulty in the precise control of dopant level and position in the

lattice [22, 23]. Pulsed laser deposition (PLD) is a versatile physical technique offering a wide range of tunable deposition parameters (e.g. energy and flux of species impinging the substrate) that enables the fine control of thin film microstructure, hence properties [24]. Moreover, PLD allows the deposition of multilayered films with good adhesion to substrates and high quality at interfaces without requiring complex steps and chemical binders [25]. In addition, PLD provides high surface quality (no contamination) as compared to chemical methods. Finally, the film thickness and doping amount – which are crucial in the fabrication of multilayered gradient nitrogen doped films- can be precisely controlled by varying the laser pulse number and the ratio between N_2 and O_2 gases in the deposition chamber, respectively.

To the best of our knowledge, most of the research works on gradient-doped semiconductors have so far been focused on harvesting and converting solar energy to clean and storable chemical [10, 17, 19, 26] or electrical energy [14, 16], while their application in environmental purification – whereas both electrons and holes would participate in the photocatalytic degradation– has not been reported. Herein, we used PLD technique for the fabrication of N-doped TiO_2 with the anatase phase at different doping levels of substitutional nitrogen into the TiO_2 lattice. Furthermore, a unique, multiple-homojunction structure composed of six layers of gradient doped anatase TiO_2 with a columnar-like morphology (g-N-TiO_2) was fabricated and its photocatalytic performance was compared with that of pristine TiO_2 and N-TiO_2 (non-gradient) in terms of photoelectrochemical (PEC) properties and SMX removal in aquatic media.

2. Experimental procedure

2.1. Photocatalyst preparation

In this study, N-doped anatase TiO_2 samples with different amounts of nitrogen were prepared by using the PLD method. A KrF excimer laser (λ=248 nm, 10 Hz repetition rate, pulse width=25 ns)

was used to ablate a rotating Ti target (99.995% purity, Kurt J. Lesker, USA). The pulse energy density (fluence) at the target surface was 4 J/cm^2. The target was moved and rotated continuously across the laser beam to minimize pitting. The target-to-substrate distance was fixed at 6.5 cm and the synthesis was performed at a substrate temperature of 350 °C in either high purity O_2 gas (for TiO_2 deposition) or in a mixture of high purity N_2 and O_2 gas (for nitrogen doped TiO_2 deposition). By changing the N_2:O_2 ratio from 10:90 to 90:10 at a constant deposition pressure, the N-TiO_2 samples were prepared and labelled as 10N to 90N, respectively. The substrates were ultrasonically cleaned in acetone, isopropanol and de-ionized water for 10 min successively, and then dried under N_2 stream before deposition. In the next step, gradient doped TiO_2 (g-N-TiO_2) was fabricated by layer-by-layer deposition of N-TiO_2 with different amounts of doped nitrogen on fluorine doped tin oxide (FTO) and polished Si (100). As illustrated in Fig. 1, the first layer deposited on FTO was undoped TiO_2, while the nitrogen content of the deposition gas (N_2:O_2 mixture) was increased for the next layers, successively. For comparison, TiO_2 (without doping) and N-TiO_2 (prepared with N_2:O_2=90:10) were also prepared with the similar thickness of g-N-TiO_2. The thickness of each layer (~90 nm) of the multi-layer g-N-TiO_2 sample was controlled by varying the pulse number during laser deposition.

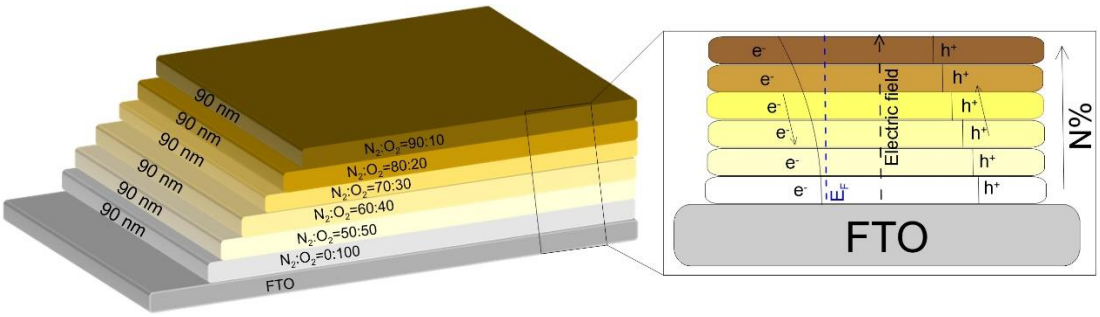

Fig. 1. Schematic and energy level diagrams of multi-layer g-N-TiO_2.

2.2. Characterization instruments

A PANalytical X'Pert MRD, equipped with a Ni-filtered CuKα radiation source operated at 45 kV and 40 mA was used to analyze the crystalline structure of samples in the range of 20-80° and determine their density by X-ray reflectometry (XRR). Accordingly, XRR θ-2θ within the range of 0.1–3° were recorded. The density of films (ρ_{film}) is calculated using the following equations [27]:

$$\rho_{el} = \frac{\theta_c^2 \pi}{\lambda^2 r_{el}} \quad (1)$$

$$\rho_{film} = \frac{A\,\rho_{el}}{N_A Z} \quad (2)$$

where ρ_{el} is the electron density, θ_c is the critical angle, λ=1.5406 Å is the wavelength of X-ray radiation source, $r_{el}=2.81\times10^{-6}$ nm is electron radius, N_A is the Avogadro number, A and Z are atomic mass and number respectively. A VG Escalab 220I-XL photoelectron spectrometer, equipped with an AlKα radiation monochromatic source ($h\upsilon$ = 1486.6 eV) was used to evaluate the elemental characteristics after performing *in-situ* surface etching of samples by a 5 keV Ar^+ ion sputtering gun. The morphology of samples was observed by a JEOL JSM-7401F scanning electron microscope (SEM). A Nanoscope III atomic force microscope (AFM) from Digital Instrument was used to investigate the surface morphology and roughness. The UV-Vis absorption spectra of the samples were measured with a UV-vis-NIR absorption spectrometer (Varian Cary 5000). PEC experiments were conducted in a three-electrode cell with the photocatalysts deposited on FTO as the working electrode, while Ag/AgCl electrode and platinum (Pt) wire were used as reference and counter electrodes. The 0.2 M Na_2SO_4 aqueous solution was used as the electrolyte during PEC tests. An electrochemical workstation (CHI 660E, CH Instruments) equipped with a 300 W Xe lamp solar simulator (LCS-100, Newport) was used for photocurrent-time (I-t), photocurrent–potential (I-V) measurements and electrochemical impedance spectroscopy.

2.3. Photocatalytic removal experiment

SMX was purchased form Sigma-Aldrich Inc., USA. SMX stock solution (1 mg/L) was prepared by using deionized Milli-Q water (18 μS cm^{-1}). A photoreactor was designed which consists of a cell, a sample holder (1 inch × 1 inch), a quartz window (5 cm diameter) and an external reservoir for sampling. The initial volume of solution was 50 mL. The solution in the cell was circulated by a peristaltic pump operated at a constant 250 mL/min flow-rate. Before turning on the solar simulator, the solution was circulated for 30 min to achieve adsorption-desorption equilibrium between the photocatalyst film and SMX. The samples were illuminated by a solar simulator (ABET 2000) during the photocatalytic experiments. During each photocatalytic experiment, about 1.5 mL of the solution was collected at different time intervals for ultra-high performance liquid chromatography (UHPLC) analysis. For comparison, the photolysis experiment was conducted under the similar condition in the absence of the photocatalyst film. Before all experiments, the solar simulator was turned on for 30 min to ensure a stable light intensity. The removal percentage of SMX was calculated by Eq. (3):

$$Removal\ (\%) = (1 - \frac{C_t}{C_0}) \times 100 \quad (3)$$

Pseudo-first-order kinetic model was used to determine the kinetic constants for each photocatalyst [28]:

$$-\ln \frac{C_t}{C_0} = kt \quad (4)$$

where C_0 (μg/L) is the initial concentration of SMX, C_t (μg/L) is the concentration at time t, and k is the reaction rate constant (min^{-1}). After treatment, the photocatalysts were cleaned for 5 min in deionized water under mild sonication, washed several times, and dried at 50 °C to be used in cyclic experiments.

2.4. Analytical measurement and transformation products identification

The SMX concentration measurement and the identification of the transformation products (TPs) were performed by using a Nexera UHPLC system (Shimadzu, Columbia, MD). Accordingly, 1 µL of samples were injected into a Phenomenex Kinetex C18 column (2.1 × 50 mm, 1.7 µm) at the column temperature of 40 °C. The mobile phase was (A) water with 0.1% formic acid and (B) acetonitrile with 0.1% formic acid at the flow rate of 0.3 mL/min. A linear gradient was used starting with 97% (A) for one minute, changing to 50% (A) for 15 minutes and then 15% (A) for 18 minutes. Data were acquired in information-dependent acquisition (IDA) mode, with time-of-flight mass spectrometry (TOF-MS) survey acquisition from *m/z* 80–925, followed by MS/MS on the 3 most intense ions from *m/z* 200–450 with dynamic background subtraction with a total cycle time of 1.0 s. The MS and MS/MS spectra were collected on a hybrid quadrupole-time-of-flight (QqTOF) TripleTOF 5600 mass spectrometer (SCIEX, Concord, ON, Canada) equipped with a DuoSpray ion source in the positive ion mode set at 5 kV source voltage, 450 °C source temperature, and 50 psi for GS1/GS2 gas flows. QqTOF offers abundant structural information with high sensitivity for unknown compound analysis without the need to use standards, which are rarely available [12].

2.5. Toxicity assessment

The performance of synthesized photocatalysts in terms of solution detoxification was evaluated by comparing the toxicity of the antibiotic solutions before and after photocatalytic treatment with TiO_2, N-TiO_2 and g-N-TiO_2 in term of optical density measurement [29]. Accordingly, five test groups were conducted as follows: (i) the control group (4 mL Lysogeny broth (LB) medium mixed with 4 mL deionized water), (ii) the untreated solution group (4 mL LB medium mixed with 4 mL initial SMX solution without any photocatalytic treatment), (iii) the treated group with TiO_2 (4 mL

LB medium mixed with 4 mL treated solution with TiO_2 for 300 min), (iv) the treated group with N-TiO_2 (4 mL LB medium mixed with 4 mL treated solution with N-TiO_2 for 300 min), and (v) the treated group with g-N-TiO_2 (4 mL LB medium mixed with 4 mL treated solution with g-N-TiO_2 for 300 min). Two parallel experiments were conducted in each group. Afterward, the solutions were kept at 37 °C for 3h and 1 mL (~1×10^8 CFU/mL) JM103 *Escherichia coli* (E. coli) was added to each solution and incubated at 37 °C. After 3h and 6h the optical density value of culture at 600 nm (OD_{600}) was measured by using a UV–vis spectrophotometry. The growth of bacteria colonies on the agar surface was monitored to visualize the change of toxicity of the solution before and after treatment [30]. Accordingly, ~400 μL of solutions, which were incubated for 6h with the previous method, were spread over the surface of the agar that had been prepared by mixing the appropriate amount of agar and nutrient broth. After incubation overnight at 37 °C, the number of grown *E. coli* colonies on the surface of agars was counted.

3. Results and discussion

3.1. Structural characterization

The composition of the fabricated nitrogen doped TiO_2 films was evaluated by X-ray photoelectron spectroscopy (XPS). Fig. 2(a) illustrates the XPS survey spectra of TiO_2 and sample 90N before Ar^+ etching (for easier comparison, only TiO_2 and 90N XPS spectra are presented in Fig. 2). From the survey scan, XPS peaks related to Ti, O, N and adventitious C were observed for the as-prepared 90N sample. The Ti2p spectra in Fig. 2(b) show that the as-prepared undoped TiO_2 consists of two Ti^{4+} located at 459.5 and 465.3 eV, which agrees with the literature [31], while these two peaks are slightly shifted to 459.2 and 465.0 eV after nitrogen doping [32]. This slight shift is due to an increase of the electron density on Ti as a result of the partial replacement of nitrogen with oxygen which shows a higher

electronegativity [32]. A similar trend is also shown for the O1s XPS spectra as illustrated in Fig. 2(c). The presence of nitrogen into the lattice also shifts the O1s peaks from 532.2 and 530.8 eV to 531.9 and 530.5 eV, which correspond to the bridging hydroxyls and lattice oxygen respectively [31].

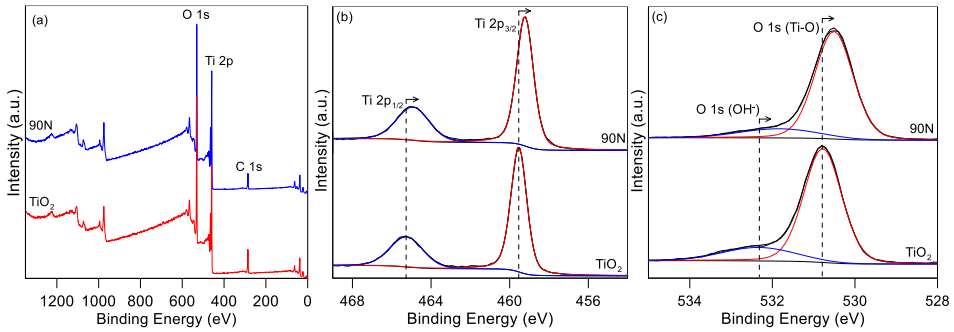

Fig. 2. (a) XPS survey spectra, (b) XPS spectra of Ti2p and (c) XPS spectra of O1s of TiO_2 and sample 90N.

The accurate content of nitrogen was calculated after Ar^+ etching of the sample surface for 600 s to remove contaminants, if there were any. The high-resolution XPS spectra of N1s peaks of 10N to 40N thin films are presented in Fig. 3(a). As seen, at low N_2:O_2 ratios, two N1s peaks located above 400 eV are present which are assigned to chemisorbed molecular nitrogen (N-O and N-C) or interstitially doped nitrogen [9]. As illustrated in Fig. 3(b), by increasing the N_2:O_2 ratio, an additional N1s located at 396 eV appears for 50N-90N samples, which corresponds to substitutional N doping [20]. Some researchers have concluded that only substitutional doping leads to an increase of photocatalytic activity [33-35]. Farkas et al. [9] reported that substitutional N doping is responsible for shifting the absorption edge to lower photon energies and reducing the band gap of TiO_2.

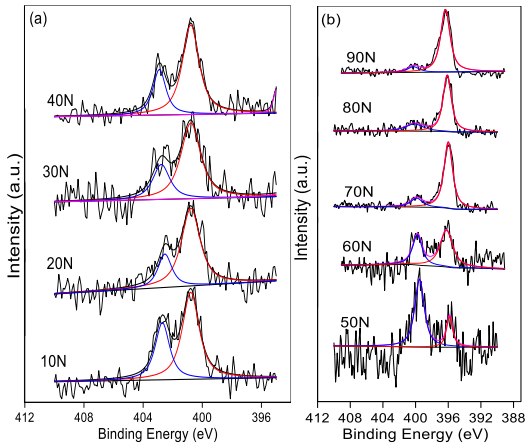

Fig. 3. (a) High-resolution N1s XPS spectra of the N-doped TiO_2 films prepared in N_2:O_2 ratio lower than 50% (10N-40N), and (b) equal to or higher than 50% (50N-90N) after 600s Ar^+ etching.

Fig. 4(a) shows the XRD patterns of 50N-90N samples as well as pristine TiO_2. As mentioned before, all depositions were performed at 350°C without any post-annealing step. The distinct and sharp peaks for all the samples confirm the crystalline nature of TiO_2 films. The peaks at 25.4°, 38.1°, 48.1°, 54.5°, 55.2°, 62.7°, 69.2° and 70.5° could be assigned to the (101), (004), (200), (105), (211), (204), (116) and (220) planes of anatase TiO_2, respectively (JCPDS file No. 21-1272) [36]. No additional peaks were detected in the XRD pattern of pristine and N-doped TiO_2, confirming the high purity of the synthesized anatase TiO_2 films. The lack of common anatase to rutile phase transformation after nitrogen doping in this study might be due to either substitutional doping (rather than interstitial doping) and/or the low amount of N doping in the structure. It is reported that the anatase phase of TiO_2 possesses a higher photocatalytic activity compared to the rutile and brookite phases [37]. The higher photocatalytic activity of the anatase phase can be explained by the longer lifetime of charge carriers in this phase [38]. The high-temperature nitridation treatment of TiO_2 is a widely-used method for the incorporation of nitrogen into the TiO_2 lattice although high temperature causes the formation of unwanted side phases, defects, as well as degradation of the FTO substrate and sintering of the nanostructure [35]. The method

proposed in this work leads to the substitution of oxygen by nitrogen in the anatase TiO_2 in a controlled manner and without phase change. As seen, all peak intensities are decreased by increasing the nitrogen to oxygen ratio during the film deposition. This results from the reduction of the film crystallinity by the incorporation of N into TiO_2 [9]. Nonetheless, even the 90N sample was crystalline and the (101) diffraction peak could be distinguished. This finding is inconsistent with some research works, where doping nitrogen into TiO_2 lattice led to an amorphous structure [9, 39]. Fig. 4(b) shows the enlarged view of the (101) peak of TiO_2 and 50N-90N samples. Due to the slightly larger radius of N compared to O, this peak slightly shifts towards a lower angle after nitrogen substitution, confirming that N is successfully incorporated into the anatase TiO_2 lattice [10].

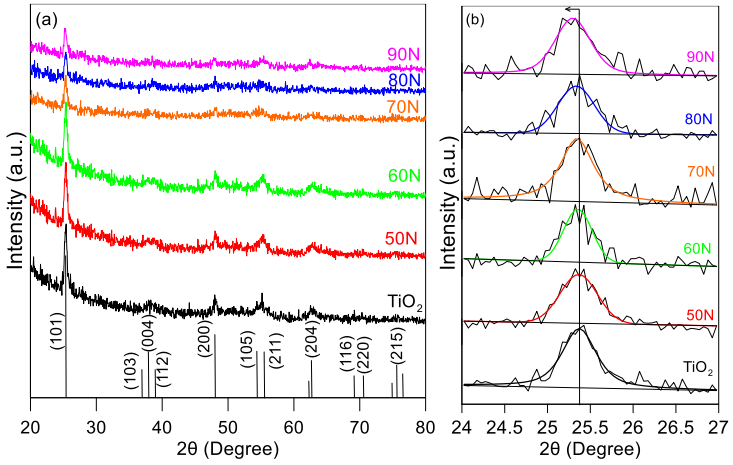

Fig. 4. (a) XRD patterns of the films deposited at 350 °C substrate temperature at different N_2:O_2 ratio (50N-90N); (b) enlarged XRD patterns showing the (101) diffractions of the samples changed from 24° to 27°.

3.2. Optical properties

It is proven that nitrogen doping introduces impurity levels within the forbidden band gap and extends the optical absorption edge of TiO_2 to the visible range [17]. Nitrogen doping has a

profound effect on the photocatalytic performance of semiconductors. However the underlying principles behind its mechanism are still not fully understood [20, 40, 41]. Fig. 5(a) illustrates the UV-Vis absorption spectra of pristine and N-TiO_2 films. After N doping, the optical absorption edges of TiO_2 show a red shift, indicating a better optical absorption capability of N-doped TiO_2 in the visible light range. As illustrated in Fig. 5(a), increasing the N_2 content in the N_2:O_2 mixture from 0 to 40% (bare TiO_2, 10N-40N) also slightly increases absorption in the visible range, although a notable light absorption enhancement is only achieved above 50% of N_2 in the N_2:O_2 mixture (enlarged in Fig. 5(a)). As confirmed by XPS results, below 50% N_2, mainly interstitial nitrogen doping (~400 eV) is obtained and the signal supporting substitutional nitrogen doping (~396 eV) only emerges above 50% N_2 content. Comparing two types of N-TiO_2, Lynch et al. [20] reported that samples with a higher percentage of substitutional nitrogen yield a higher light absorption and a lower band gap. The band gap energy of TiO_2 can be calculated by the Tauc plot from the intercept of the tangent fitted to the $(\alpha h\vartheta)^{1/2}$ vs $h\vartheta$ plot [9, 18] as shown in Fig. S1 in the Supporting Information. The band gap of pristine TiO_2 was determined as 3.2 eV, which is consistent with the reported value for anatase TiO_2 in the literature [8]. As seen, the band gap of N-doped TiO_2 is reduced to 3.1, 3.0, 2.9, 2.8 and 2.6 eV for 50N, 60N, 70N, 80N and 90N, respectively. The relationship between the amount of substitutional nitrogen doping and the band gap of TiO_2 is depicted in Fig. 5(b). As shown in Fig. S2, bare TiO_2 film is highly transparent while by increasing the N_2:O_2 ratio, the color gradually changes to brownish, which is consistent with UV-Vis absorption results. Since a meaningful enhancement in UV-Vis absorption was obtained by substitutional nitrogen doping, samples 50N-90N were selected for the fabrication of gradient-doped TiO_2 in the ensuing experiments.

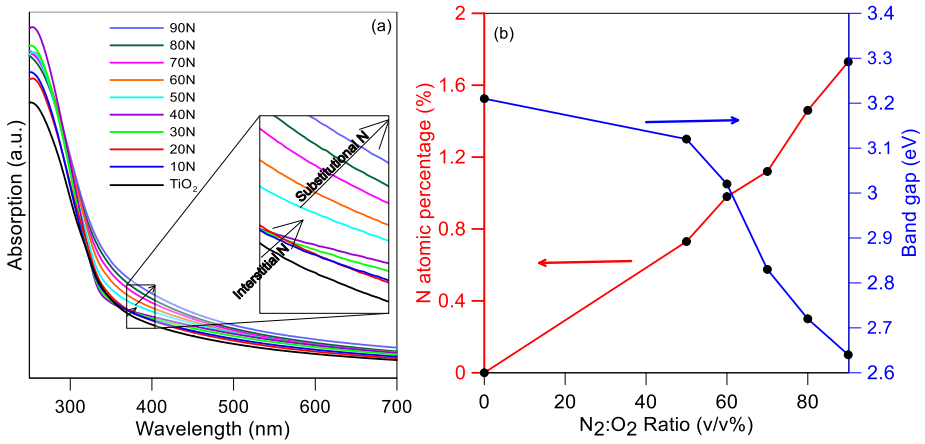

Fig. 5. (a) UV–Vis absorption spectra of various samples prepared at different N_2:O_2 ratios (10N-90N), (b) changing of the N atomic percentage and band gap of TiO_2 by N_2:O_2 ratio during deposition.

3.3. Morphological structure

The reproducibility as well as the precise film thickness and composition control represent three significant advantages of the PLD compared to the wet chemical methods [23, 42]. Moreover, the morphology, orientation and porosity of the film can be controlled by tuning the deposition parameters, such as working pressure and substrate temperature [23]. In this study at a constant substrate temperature (350°C), the g-N-TiO_2 films were deposited at three different pressures (10, 20 and 30 Pa). As seen in Fig. 6(a-b), the g-N-TiO_2 sample fabricated at 20 Pa pressure exhibits a vertically aligned columnar-like nanostructure, while the sample prepared at 10 Pa is compact and dense (Fig. S3(a)). By increasing the deposition pressure (30 Pa), the sample changes from a columnar-like to a disordered structure composed of nanoparticles (Fig. S3(b)). This is because the kinetic energy of the ablated species decreases due to their collisions with the nitrogen and oxygen gas molecules. Actually, the kinetic energy of ablated species determines the morphology, orientation and porosity of film [43]. At 10 Pa, the ablated species have a high kinetic leading to the densification of the thin film. In contrast, at 30 Pa, the ablated species experience multiple collisions before reaching the substrate, resulting in the formation of a film with loose interparticle

connections (as seen in Fig. S3(b)). The surface roughness (root mean square roughness measured by AFM), was ~3 nm for the sample prepared at 10 Pa (Fig. 6(c-d)) which increased to ~7 nm and ~10 nm by increasing the deposition pressure to 20 Pa and 30 Pa (Fig. S4). By using the XRR method (Fig. S5), the density of the deposited samples at 10, 20 and 30 Pa were calculated to be 3.16, 2.91 and 2.56 g/cm^3, which corresponded to film porosities of 19.2%, 25.6% and 34.5%, respectively. It is clear that the films are less compact as compared to the anatase TiO_2, which has a reported density of 3.91 g/cm^3 [44]. Differential reflected X-ray intensity graph (Fig. S6) was used for the precise measurement of the critical angle since the accuracy of density measurements by using XRR method highly depends on the critical angle accuracy. It is reported that increasing the porosity can enhance the specific surface area and the number of active catalytic sites and also, increase the light absorption by the formation of scattering centers inside the porous structures [26]. Highly porous photocatalysts suffer from the lack of robustness and possess high trap states and interfacial recombination centers, whereas one-dimensional columnar-like TiO_2 structure reduces charge recombination rate, resulting in enhanced charge-collection efficiency [43]. Compared to the columnar-like structure (prepared at 20 Pa), the dense film (prepared at 10 Pa) as well as the film composed of loosely attached nanoparticles (prepared at 30 Pa) hindered the charge carrier separation by bulk or boundary recombination of charge carriers as was confirmed by the higher PEC results for samples prepared with different density by the PLD process (Fig. S7). More details are provided in Section 3.4.

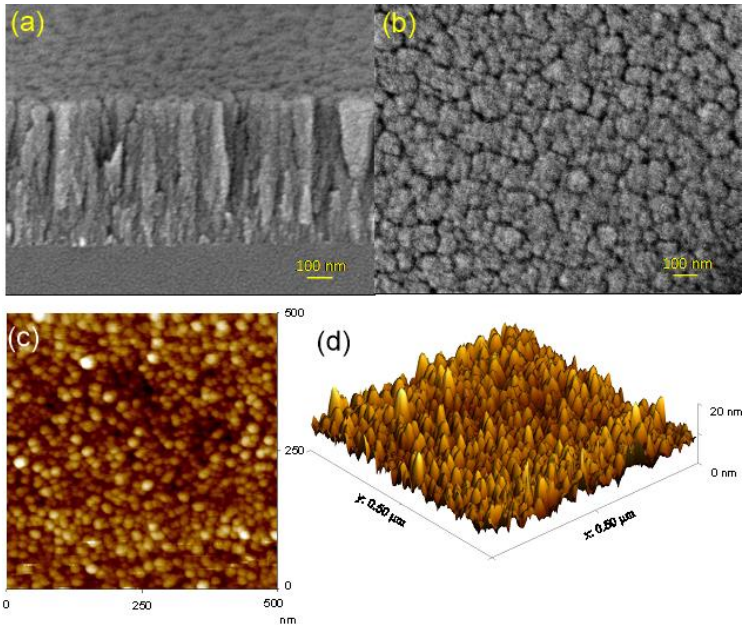

Fig. 6 (a) Side view and (b) top view SEM images; (c, d) AFM topographic image of g-N-TiO_2 film prepared at 20 Pa.

3.4. Photoelectrochemical performance

The effects of morphology on the photoelectrochemical performance of semiconductors were reported in several studies [26, 44, 45]. Noh et al. [43] concluded that vertically-aligned one-dimensional structure has a profound effect on the electron dynamics of dye-sensitized solar cells. One-dimensional columnar-like structures have several advantages, such as increased surface-area-to-volume ratio and stronger light trapping capability, as compared to compact films. In addition, with an anisotropic morphology, similar to nanowires and nanotubes, the charge transfer along the vertically-aligned direction is facilitated and the mass transfer limitation is reduced by providing readily accessible porosity for diffusion of contaminant molecules and/or hydroxyl ions to generate highly reactive hydroxyl radicals ($^{\bullet}OH$) [44]. Fabricating one-dimensional TiO_2 by PLD, Sauvage et al. [45] reported an increase by more than one order of magnitude in the lifetime of photo-induced electrons compared to a TiO_2 film consisting of 20 nm nanocrystalline particles.

In the present work, in order to investigate the effect of film density on the photocatalytic activity, the PEC performance of g-N-TiO_2 prepared at 10, 20 and 30 Pa was evaluated. As seen in Fig. S7(a), by increasing the deposition pressure from 10 to 20 Pa and changing the morphology from dense to columnar-like nanostructure, a considerable improvement of the photocurrent density was obtained in cyclic on/off current-time (I-t) experiment. As mentioned before, the sample prepared at 10 Pa possesses a dense structure leading to the bulk recombination of electron and holes. Furthermore, the light harvesting might be limited for dense structure compared to porous films [46]. A low photocatalytic activity of dense TiO_2 prepared by PLD was also previously reported [44]. The highest photocurrent was achieved for the sample prepared at 20 Pa. With further pressure increased to 30 Pa, the photocurrent density dropped considerably due to the high recombination rate of electrons and holes at numerous nanoparticles' boundaries. Fig. S7(b) shows the linear sweep voltammetry (LSV) photocurrent density under on/off cyclic conditions. All the samples showed negligible dark current in the positive applied bias voltage vs. Ag/AgCl. In accordance with I-t results, the sample prepared at 20 Pa showed the highest current density in LSV experiment under one sun irradiation. The sample prepared at 30 Pa obtained the lowest current density despite of its higher porosity which allows a deeper penetration of electrolyte into the film and perhaps, more absorption due to multiple scattering. As seen in Fig. S3(b), for the film prepared at 30 Pa, the physical contact between the nanoparticles is not good enough for efficient electron transfer, which provides a higher chance of electron trapping at the interface between the TiO_2 nanoparticles [43, 47]. The dark and illuminated Nyquist plots of electrochemical impedance spectroscopy (EIS) are illustrated in Fig. S7(c). A lower diameter of semicircle of EIS plots under dark and illuminated conditions further confirms the lower charge transfer resistance of the g-N-TiO_2 sample prepared at 20 Pa. For the sample prepared at 20 Pa,

the photocurrent in the I-V curve experienced sharp anodic spikes (positive current transients) after the light was switched on, which is due to the accumulation of photo-induced holes at the photocatalysts/electrolyte interface without electrolyte injection [10]. These anodic spikes became less evident at higher potentials where the applied bias forced the photo-induced holes to inject to the electrolyte [48]. The anodic spikes could be an evidence of facile transport of holes to the interface where the photo-induced holes encounter the injection barrier. As demonstrated in Fig. S8, once the 0.5M H_2O_2 as hole scavenger added to the electrolyte, the positive current transients vanished. Moreover, as expected, the addition of H_2O_2 to the electrolyte resulted in an improvement of photocurrent density, which further confirmed the presence of the injection barrier [49]. In this study, the samples prepared at 20 Pa provided the best morphology and PEC performance. Therefore, TiO_2, N-TiO_2, and g-N-TiO_2 samples were deposited on FTO at 20 Pa to evaluate the effect of gradient doping on PEC and photocatalytic performance. Fig. 7(a) depicts the photocurrent–time (I–t) plot of TiO_2, N-TiO_2 and g-N-TiO_2 samples under intermittent on–off illumination. Under one sun irradiation and by applying 0.2 V vs. Ag/AgCl bias and in 0.2 M Na_2SO_4 solution, the maximum photocurrent density of ~0.028 mA/cm^2 was achieved for the g-N-TiO_2 photoanode which is about 211% and 102% higher than that of the pristine TiO_2 and N-TiO_2, respectively. The photoanodes revealed an instantaneous decay of the photocurrent in dark condition and a rapid recovery to the initial photocurrent density under illumination in multiple on/off cycles, which is attributed to the fast charge carrier transport in the one-dimensional structure. The dark photocurrent density for all the photoanodes was ~0.1 μA/cm^2 at a bias of 0.2 V vs Ag/AgCl, indicating that the measured photocurrent was exclusively due to the photo-induced charges from the photoanodes.

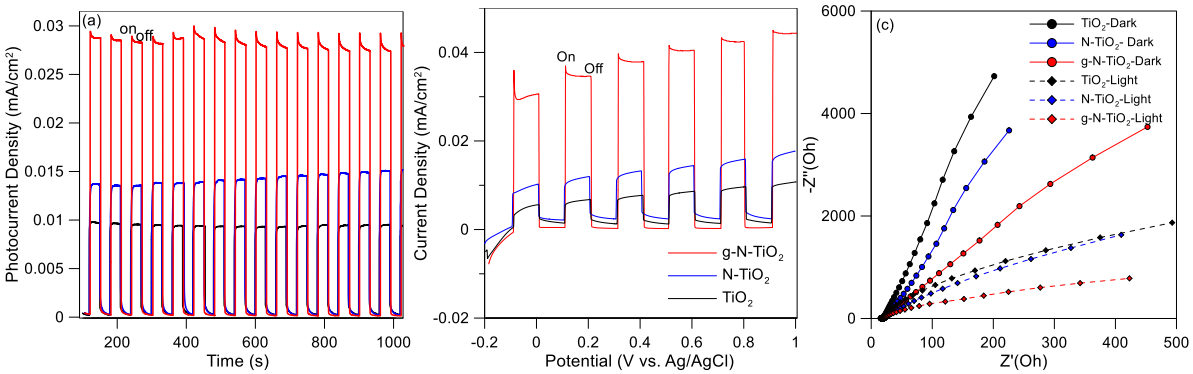

Fig. 7. (a) On/off cycle of photocurrent density (I-t) performed in 0.2 M Na_2SO_4 solution, (b) chopping linear sweep voltammetry (LSV) curves and (c) Nyquist plots of EIS measurements of TiO_2, N-TiO_2 and g-N-TiO_2. 0.2 V vs. Ag/AgCl was applied for I-t and EIS experiments.

Fig. 7(b) shows the I-V plot of samples under cyclic dark and illumination conditions. The photocurrent density of all the samples was enhanced by increasing the applied potential, indicating the typical photoelectrochemical property of n-type semiconductors. Similar to I-t results, while the dark current was insignificant, a notable photocurrent density was gained for the g-N-TiO_2 sample by applying a positive bias vs. Ag/AgCl and one sun irradiation, which was significantly higher than those achieved by N-TiO_2 and TiO_2 samples. EIS Nyquist measurements were also conducted under dark and illuminated conditions to observe the electrical resistance. A notable decrease in the diameter of N-TiO_2 was observed and the lowest diameter was obtained for the g-N-TiO_2 sample, which further confirms a lower resistance of g-N-TiO_2 against charge carrier transfer as a result of terraced band bending. As mentioned before, TiO_2, N-TiO_2 and g-N-TiO_2 samples are prepared at a similar deposition condition and possess similar density (2.91 g/cm^3). The UV-Vis spectra of these samples are shown in Fig. S9. Interestingly, despite a slight lower light absorption of g-N-TiO_2 compared to N-TiO_2 sample, the photocatalytic activity of g-N-TiO_2 was significantly higher than that of TiO_2 and N-TiO_2 samples. Therefore, it can be inferred that this improvement is mainly due to the enhanced separation of photo-induced electrons

and holes by the formation of homojunction with terraced band bending. It is proven that nitrogen as a non-metal dopant, introduces an acceptor level above the valance band of TiO_2 as a n-type semiconductor and lowers the Fermi level (E_F) of TiO_2 [35]. Therefore, a band bending is induced when different layers (with different E_F) are brought into contact [13, 14]. For non-gradient nitrogen doped sample (N-TiO_2), the band bending is limited to a narrow region at the semiconductor/electrolyte interface (depletion region) [50]. However, in g-N-TiO_2 sample, after contacting N-TiO_2 layers with different N content, the Fermi energy levels equilibrate by flowing the electron from nitrogen rich layers to layer with lower nitrogen content and finally the pristine TiO_2 layer [10]. More importantly, in gradient-doped TiO_2, the terraced valence band level for different layers induces a built-in electric field perpendicular to the substrate, which facilitates the transfer of charge carriers by repelling the electrons and holes in different directions along the vertical direction of columnar-like structure [14, 16, 17]. By measuring the electron conductivity of homogenously doped and gradient-doped hematite (α-Fe_2O_3), Luo et al. [50] concluded that the built-in electric field is responsible for the enhanced photocurrent generation. Fabrication of a heterojunction to induce band bending is a well-established strategy to promote the charge separation in photocatalysis even though a higher efficiency of gradient doped homojunction was demonstrated in recent years [10, 14, 16, 17, 19, 21, 26, 51]. In contrast to heterojunction –where the band bending is limited to the interfaces– the gradient-doped homojunction distributes the band bending over a larger region in the bulk of the sample and thus, promotes the charge separation efficiency [13, 14]. Moreover, lattice mismatch and interfacial defects are intrinsically reduced for gradient-doped TiO_2 homojunction prepared by PLD due to layer-by-layer epitaxial growth of TiO_2 with the sample lattice parameters but different E_F. In other words, gradient-doped homojunction structure distributes a moderate band bending over the photocatalyst's bulk without

interfacial defects between layers. It is reported that the lattice matching in homojunction facilitates the spatial transfer of the photo-induced electron and holes and reduces the electrical resistance in the photocatalyst structure [18]. To evaluate the stability of g-N-TiO_2 photocatalysts, the long-term I-t experiment under one sun irradiation was carried out. As shown in Fig. S10 in the Supplementary Information, no significant decline in the current density was shown within 8 h, suggesting the high stability of g-N-TiO_2 sample.

3.5. Photocatalytic performance

Considering the low specific surface area of thin films, the photocatalytic removal efficiency of contaminants in water is usually low in comparison with slurry systems containing nanoparticles. In order to suppress the recombination of charge carriers and increase the degradation efficiency, in thin-film photocatalytic systems, an external potential bias is applied to the photocatalyst serving as the photoanode in the PEC process [52]. Despite the exciting reported results for the degradation of recalcitrant pollutants with PEC, this process requires applying electrical energy, expensive electrode materials (such as platinum) and also conductive substrate which impose high operating cost to the process. Moreover, PEC needs the addition of a relatively high concentration of salt to the solution (mostly sulfates) as electrolytes, which raises an additional environmental concern. Therefore, increasing the efficiency of thin-film photocatalysts without such costly and/or environmentally unsafe materials, is of great importance. In this study, the photocatalytic performance of photocatalysts was evaluated with the degradation of SMX antibiotic under simulated solar light irradiation. Fig. 8(a) shows the normalized degradation curve of SMX with photolysis, and photocatalysis by using TiO_2, N-TiO_2 and g-N-TiO_2 films. As seen, no significant reduction in the concentration of SMX was achieved by the photolysis process. This is because of the low absorption of light by SMX in the solar spectrum range as previously reported [53]. As

expected, the removal of SMX by pristine TiO_2 is insignificant and only ~19% SMX removal is achieved after 300 min treatment. The low removal efficiency of TiO_2 for the photocatalytic degradation is due to the low light absorption of TiO_2 in the solar spectrum. Fig. 8(b) shows that photocatalytic degradation of SMX follows a pseudo-first-order kinetics and the photocatalytic kinetic constant (*k*) by using TiO_2 photocatalyst is 0.0006 (min^{-1}). In contrast, after 300 min the removal percentage of SMX by using N-TiO_2 is ~40 % with a kinetic constant of 0.0017 (min^{-1}). The highest removal efficiency is obtained by using g-N-TiO_2 with ~85 % removal after 300 min and the kinetic constant is 0.0061 (min^{-1}) which is ten times higher than that of TiO_2 photocatalyst. The improvement in the photocatalytic degradation performance of g-N-TiO_2 is consistent with the improvement of its PEC performance. The reason of this dramatic enhancement in photocatalytic degradation efficiency is due to the promotion of charge carriers' separation by the built-in oriented electric field as a result of terraced band bending along with vertical direction of TiO_2 as reported before [17]. As shown in Fig. S8, the transferred and accumulated holes on the surface of g-N-TiO_2 can directly degrade SMX molecules by oxidizing them or indirectly by generation of reactive species such as $^{\bullet}OH$ radicals. As a result, a superior enhancement of the photocatalytic performance for g-N-TiO_2 was achieved in terms of SMX degradation, kinetics of removal, and solution detoxification. As presented in Table 1, the obtained removal efficiency in this study is among the highest reported values in previous studies of photocatalytic degradation of pharmaceuticals by using thin films. Moreover, the SMX removal efficiency after 300 min, 600 min and 900 treatments by using TiO_2, N-TiO_2 and g-N-TiO_2 in three consecutive runs was compared to evaluate the stability and reusability of photocatalysts. As seen in Fig. 8(c), all tested photocatalysts are very stable and maximum ~12 % loss in the SMX removal efficiency was shown after three cyclic experiments.

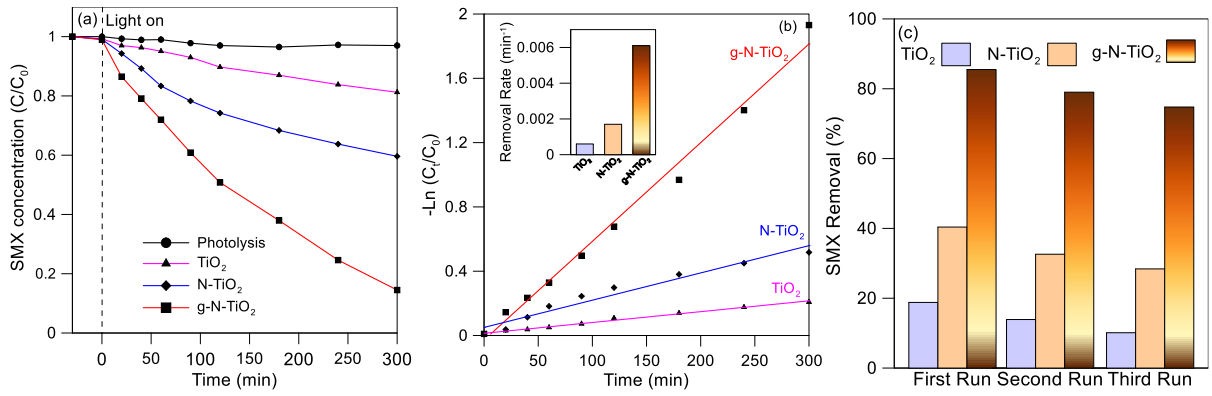

Fig. 8. (a) Normalized degradation curves of SMX by TiO_2, N-TiO_2 and g-N-TiO_2; (b) pseudo-first-order kinetics model, and inset: corresponding kinetic constants (k) during the photocatalytic process; (c) recycling tests of photocatalytic degradation of SMX after 300 min, 600 min and 900 min treatments by using TiO_2, N-TiO_2 and g-N-TiO_2.

3.6. Transformation product and mechanism of degradation

In order to identify the TPs during the photocatalytic degradation of SMX, first, LC–MS chromatograms of the samples obtained at different time intervals are compared with those of the untreated sample. The new peaks in the chromatograms of samples are considered as possible transformation products, and according to the "suspect screening" method [54], the MS/MS spectra of the suspected compounds are acquired and compared with the reported TPs in the literature. Accordingly, fifteen TPs were identified during the treatment by TiO_2, N-TiO_2 and g-N-TiO_2. As shown in Fig. 9(a-c), relatively short-chain TPs such as TP 107, TP 114 and TP 149 were not detected with TiO_2, while long-chain TPs such as TP 286 and TP 289 (Fig. 9 (n-o)) were not observed during treatment by g-N-TiO_2. The presence of short-chain TPs in the samples treated by g-N-TiO_2 suggests the capability of this photocatalyst to generate more reactive species such as $^{\bullet}OH$ radicals, which leads to the consecutive breaking of SMX into shorter TPs. In contrast, insufficient reactive radicals with TiO_2 and N-TiO_2 cause oxidation (but not bond cleavage) of the benzene and isoxazole rings (TP 286) and denitrification and oxidation of benzene ring as well as oxidation of the isoxazole ring (TP 289).

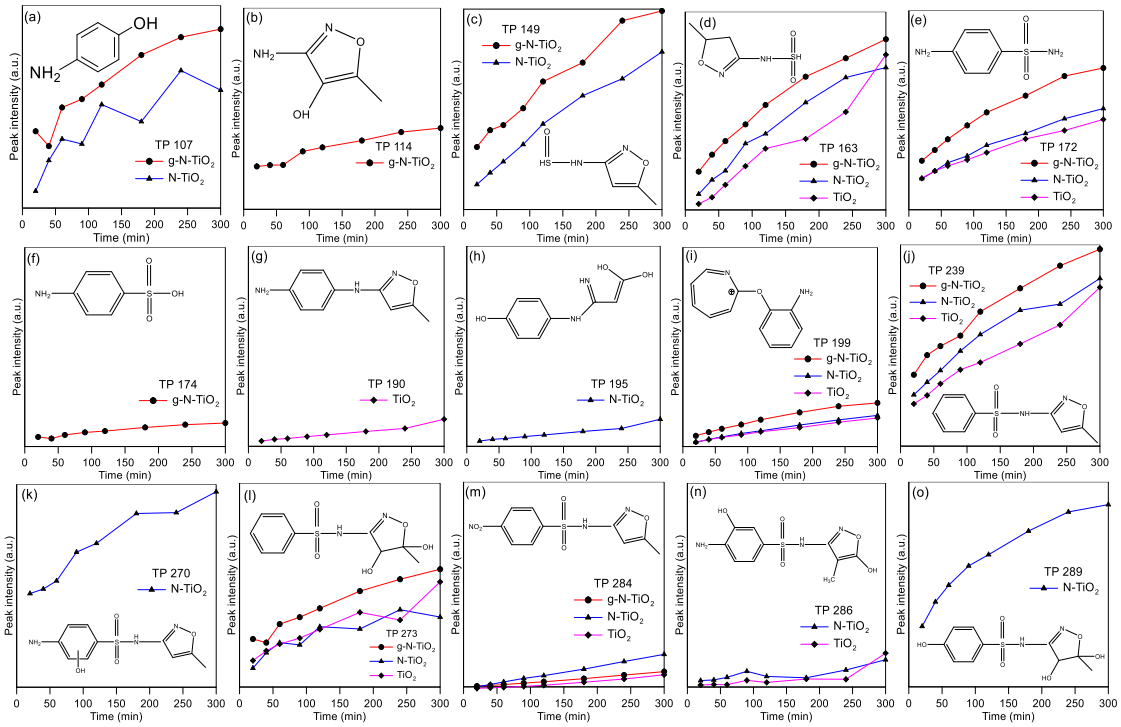

Fig. 9. Evolution of (a) TP 107, (b) TP 114, (c) TP 149, (d) TP 163, (e) TP 172, (f) TP 174, (g) TP 190, (h) TP 195, (i) TP 199, (j) TP 239, (k) TP 270, (l) TP 273, (m) TP 284, (n) TP 286, and (o) TP 289, during the photocatalytic degradation of SMX by TiO_2, N-TiO_2 and g-N-TiO_2.

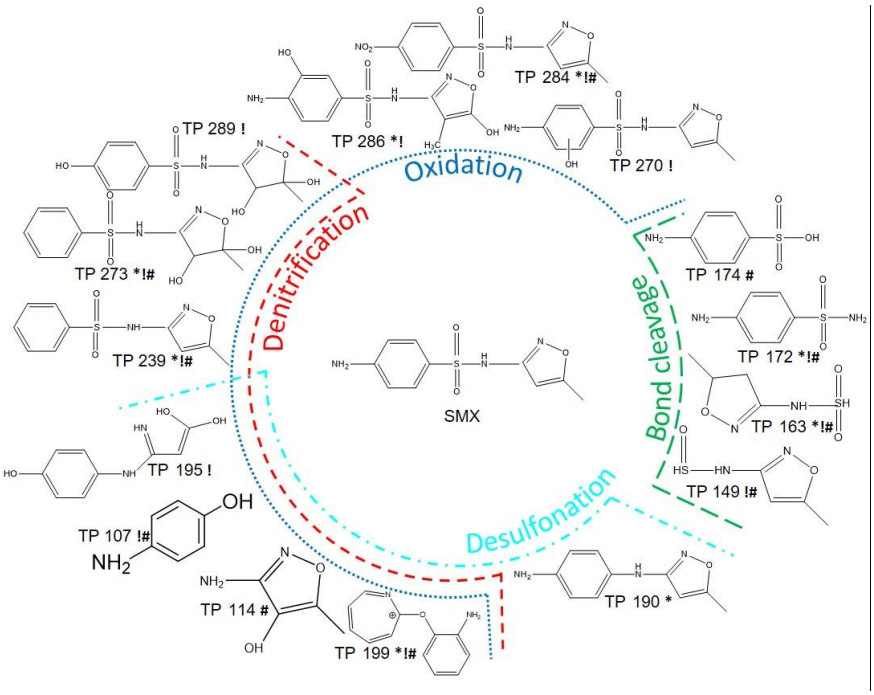

Fig. 10. Possible reaction pathway for SMX degradation including: oxidation, denitrification, desulfonation and bond cleavage. (*) detected by using TiO_2, (!) detected by using N-TiO_2 and (#) detected by using g-N-TiO_2.

The cleavage of benzene ring from sulfur (S) led to the formation of TP 163, while the breakage of isoxazole from nitrogen (N) formed TP 172. TP 163 can proceed to the formation of TP 149 by N-TiO_2 and g-N-TiO_2 and thereafter, to TP 114 by g-N-TiO_2 photocatalyst. Previous studies have also proved the ability of hydroxyl radicals for oxidation of the amino group [55, 56] which is shown for TP 195 and TP 284. TPs 163 and 172 were detected for all photocatalysts although the peak intensities of these TPs by using g-N-TiO_2 were higher than that of obtained by TiO_2 and N-TiO_2. Moreover, the successive isoxazole ring cleavage and denitrification (TP 174) and further oxidation of the isoxazole ring (TP 114) were only observed by using the g-N-TiO_2 photocatalyst. This may be due to the improved ability of g-N-TiO_2 to generate reactive species and thus, to transform SMX into smaller organic compounds. TP 195 [56], TP 270 [57] and TP 289 [58] were only found by using N-TiO_2, which have been reported before as transformation products of SMX degradation. Denitrification of the benzene ring (TP 239) and further oxidation of the isoxazole ring (TP 273) were detected for all photocatalysts which have been reported in several studies [58, 59]. TP 199 was also found for all photocatalysts which has been observed in other works [60, 61]. In general, four degradation mechanism might be involved in the degradation of SMX in this study including: (i) bond cleavage; (ii) oxidation; (iii) denitrification; and (iv) desulfonation or a combination of these pathways as illustrated in Fig. 10. The ToF/MS-MS spectra of detected TPs are provided in the Supplementary Information as Fig. S11.

3.7. Toxicity assessment

As seen in Figs. 9 and 10, several TPs were formed during the photocatalytic degradation of SMX. Some research works have reported equivalent or higher toxicity of the mixture of SMX and its TPs compared to SMX alone [62, 63]. Therefore, the toxicity of the solution after treatment should

be assessed in addition to the SMX removal. Fig. 11 compares the optical density of solutions treated by TiO_2, N-TiO_2 and g-N-TiO_2 with the untreated SMX solution as well as the control sample (without SMX) at two time intervals. As expected, a high optical density (bacteria growth) was noticed for the control sample, whereas the untreated solution significantly inhibited the growth of *E. coli* bacteria. Due to the high concentration of remaining SMX in the solution, an insignificant detoxification was achieved by using TiO_2. A relatively high detoxification occurred by using N-TiO_2. Remarkably, a notable, further enhancement in detoxification was achieved for g-N-TiO_2 as photocatalyst, with considerable bacteria growth and optical density even comparable to the case without any SMX. It is to say that the effective photocatalysis of SMX by g-N-TiO_2 led to a basically non-toxic environment. The lower detoxification efficiency of the SMX solution with TiO_2 and N-TiO_2 as compared to g-N-TiO_2 might either result from the higher concentration of not-degraded SMX, or be due to the presence of some TPs with relatively similar structures to SMX (such as TP 195, TP 270, TP 286 and TP 289) which may still have antibacterial properties.

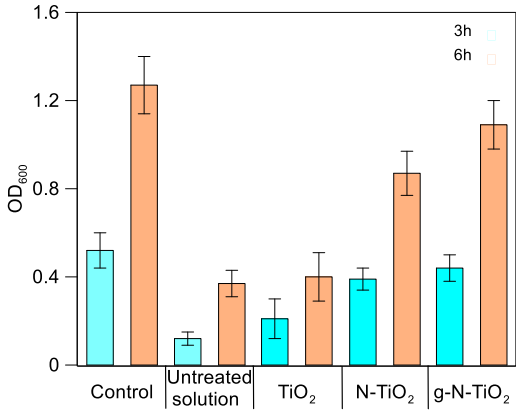

Fig. 11. Optical density measurements of *E. coli*. bacteria at a wavelength of 600 nm (OD_{600}) for samples treated by TiO_2, N-TiO_2 and g-N-TiO_2 as well as control and untreated solutions.

Fig. 12 illustrates the growth of bacterial colonies on the agar surface. As shown, the surface of agar corresponding to the control sample was completely covered by *E. coli* colonies, whereas the

untreated SMX solution (C_0) obviously hindered bacterial growth. The presence of small colonies of *E. coli* in the case of untreated SMX solution is due to the relatively low concentration of SMX in this study (initial solution), which allows bacterial growth to some extent (background growth). As seen in Fig. 12(c) in addition to the background growth, some new colonies appeared on the agar surface as indicated with red circles. However, the number of colonies was limited for the solution treated by TiO_2 consistently with the optical density (Fig. 11) and with the SMX degradation results (Fig. 8). Although a noticeable bacterial growth was observed for the treated solution with N-TiO_2, the highest detoxification was achieved for the sample treated by g-N-TiO_2. As seen in Fig. 12(e), the *E. coli* growth on g-N-TiO_2 plate was almost similar to the control petri dish, which further confirmed the high efficiency of g-N-TiO_2 for detoxification of antibiotic solution.

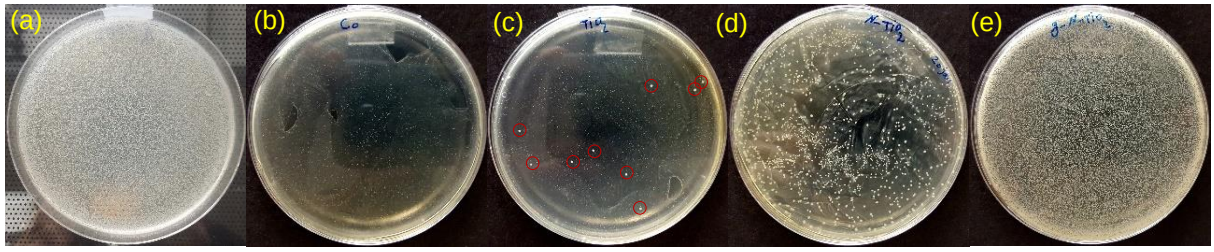

Fig. 12. Growth of *E. coli.* bacteria on petri dish for (a) control, (b) untreated SMX solutions and samples treated by (c) TiO_2, (d) N-TiO_2 and (e) g-N-TiO_2.

Table 1. Comparison of SMX removal efficiency in this study with the values reported in the literature for the removal of pharmaceuticals by using thin film photocatalysts.

Photocatalysts	Contaminants	Light source	Remarks	Ref.
Bi_2MoO_6–boron-doped diamond hybrid electrode	Ibuprofen C_0= 10 mg/L	150 W Xe lamp	• About 30% ibuprofen removal after 6h	[64]
N-doped TiO_2	Chlortetracycline C_0= 0.1 mg/L	150 W xenon lamp	• 81.3% removal after 3 h	[65]
BiOBr deposited on FTO	Tetracycline C_0= 10 ppm	(λ > 420 nm) 300-W Xe arc lamp	• 39% removal after 2.5 h	[66]

TiO_2 nano-particles decorated TiO_2 nano-tubes arrays	Diclofenac C_0= 5 mg/L	35 W Xenon lamp	• About 35% removal after 12 h	[67]
Cu/TiO_2 nanotube arrays	Diclofenac C_0= 5 mg/L	300 W xenon arc lamp	• 43.9% removal after 6 h	[68]
Reduced TiO_2 nanotube arrays	Diclofenac C_0= 5 mg/L	35 W Xenon lamp was used	• 99.5% removal after 10 h	[51]
$AgInS_2$/TiO_2 nanotube arrays	Norfloxacin C_0= 20 mg/L	500 W Xe lamp	• 46% removal after 2.5 h	[69]
Gradient Nitrogen doped TiO_2	Sulfamethoxazole C_0= 1 mg/L	300 W Xe lamp	• 85% removal after 5 h	This work

4. Conclusions

In summary, by using pulsed laser deposition, we synthesized substitutional nitrogen doped TiO_2 at low temperature without the common phase transformation of anatase to rutile. The results showed that substitutional doping is more effective than interstitial doping for enhancing light absorption by the photocatalyst. Moreover, compared to dense and highly porous structures, columnar-like structures showed more photocurrent generation and separation efficiency. Precise control of the deposition condition of the PLD allowed us to grow TiO_2 layers with different N content at the optimum deposition pressure to fabricate multi-homojunction gradient-doped TiO_2 (g-N-TiO_2). In comparison with pristine and conventional nitrogen doped TiO_2 (non-gradient), g-N-TiO_2 demonstrated a superior performance in terms of photocurrent density, SMX removal, kinetic of degradation and detoxification of solution. The obtained photocatalytic degradation efficiency obtained in the present study is as high as with a photoelectrochemical process without applying external bias potential and introducing salt as electrolyte. The markedly enhanced performance of g-N-TiO_2 is attributed to (i) substitutional nitrogen doped into the anatase phase with enhanced light absorption, (ii) fabrication of layer-by-layer homojunction with low interfacial defects, (iii) porous, well-aligned and one-dimensional structure favoring charge transport and (iv) presence of terraced band structure over the entire thickness of film, which induces an oriented electrical field and facilitates charge carrier separation and transport.

Conflicts of interest

There are no conflicts to declare.

Acknowledgements

The authors are grateful for financial support provided by Environment Damages Fund (EDF-CA-2017i001). A.M. is also grateful from the Fonds de recherche du Québec - Nature et technologies (FRQNT) for scholarship (282732). M.C. and D.M. thanks the Canada Research Chairs Program for its support.

References

[1] A. Mirzaei, F. Haghighat, Z. Chen, L. Yerushalmi, Sonocatalytic removal of ampicillin by Zn(OH)F: Effect of operating parameters, toxicological evaluation and by-products identification, Journal of Hazardous Materials 375 (2019) 86-95.

[2] Y. Yang, X. Lu, J. Jiang, J. Ma, G. Liu, Y. Cao, W. Liu, J. Li, S. Pang, X. Kong, Degradation of sulfamethoxazole by UV, UV/H2O2 and UV/persulfate (PDS): formation of oxidation products and effect of bicarbonate, Water research 118 (2017) 196-207.

[3] L. Zhou, X. Yang, Y. Ji, J. Wei, Sulfate radical-based oxidation of the antibiotics sulfamethoxazole, sulfisoxazole, sulfathiazole, and sulfamethizole: The role of five-membered heterocyclic rings, Science of the Total Environment 692 (2019) 201-208.

[4] K.K. Barnes, D.W. Kolpin, E.T. Furlong, S.D. Zaugg, M.T. Meyer, L.B. Barber, A national reconnaissance of pharmaceuticals and other organic wastewater contaminants in the United States — I) Groundwater, Science of The Total Environment 402(2) (2008) 192-200.

[5] B. Jiang, A. Li, D. Cui, R. Cai, F. Ma, Y. Wang, Biodegradation and metabolic pathway of sulfamethoxazole by Pseudomonas psychrophila HA-4, a newly isolated cold-adapted sulfamethoxazole-degrading bacterium, Applied microbiology and biotechnology 98(10) (2014) 4671-4681.

[6] X. Liu, T. Garoma, Z. Chen, L. Wang, Y. Wu, SMX degradation by ozonation and UV radiation: A kinetic study, Chemosphere 87(10) (2012) 1134-1140.

[7] Y. Min, G. He, Q. Xu, Y. Chen, Self-assembled encapsulation of graphene oxide/Ag@AgCl as a Z-scheme photocatalytic system for pollutant removal, Journal of Materials Chemistry A 2(5) (2014) 1294-1301.

[8] S.A. Ansari, M.M. Khan, M.O. Ansari, M.H. Cho, Nitrogen-doped titanium dioxide (N-doped TiO 2) for visible light photocatalysis, New Journal of Chemistry 40(4) (2016) 3000-3009.

[9] B. Farkas, P. Heszler, J. Budai, A. Oszkó, M. Ottosson, Z. Geretovszky, Optical, compositional and structural properties of pulsed laser deposited nitrogen-doped Titanium-dioxide, Applied Surface Science 433 (2018) 149-154.

[10] M. Wang, F. Ren, J. Zhou, G. Cai, L. Cai, Y. Hu, D. Wang, Y. Liu, L. Guo, S. Shen, N doping to ZnO nanorods for photoelectrochemical water splitting under visible light: engineered impurity distribution and terraced band structure, Scientific reports 5 (2015) 12925.

[11] O.T. Woo, W.K. Chung, K.H. Wong, A.T. Chow, P.K. Wong, Photocatalytic oxidation of polycyclic aromatic hydrocarbons: Intermediates identification and toxicity testing, Journal of Hazardous Materials 168(2) (2009) 1192-1199.

[12] A.G. Trovó, R.F. Nogueira, A. Agüera, C. Sirtori, A.R. Fernández-Alba, Photodegradation of sulfamethoxazole in various aqueous media: persistence, toxicity and photoproducts assessment, Chemosphere 77(10) (2009) 1292-1298.
[13] F.F. Abdi, L. Han, A.H. Smets, M. Zeman, B. Dam, R. Van De Krol, Efficient solar water splitting by enhanced charge separation in a bismuth vanadate-silicon tandem photoelectrode, Nature communications 4 (2013) 2195.
[14] F. Wang, W. Septina, A. Chemseddine, F.F. Abdi, D. Friedrich, P. Bogdanoff, R. van de Krol, S.D. Tilley, S.P. Berglund, Gradient self-doped CuBi2O4 with highly improved charge separation efficiency, Journal of the American Chemical Society 139(42) (2017) 15094-15103.
[15] Y. Li, Z. Liu, J. Li, M. Ruan, Z. Guo, An effective strategy of constructing a multi-junction structure by integrating a heterojunction and a homojunction to promote the charge separation and transfer efficiency of WO3, Journal of Materials Chemistry A 8(13) (2020) 6256-6267.
[16] T. Wu, C. Zhen, H. Zhu, J. Wu, C. Jia, L. Wang, G. Liu, N.-G. Park, H.-M. Cheng, Gradient Sn-Doped Heteroepitaxial Film of Faceted Rutile TiO2 as an Electron Selective Layer for Efficient Perovskite Solar Cells, ACS applied materials & interfaces (2019).
[17] Y. Liu, F. Ren, S. Shen, J. Chen, Y. Fu, G. Cai, X. Wang, Z. Xing, L. Wu, X. Zheng, Vacancy-doped homojunction structural TiO2 nanorod photoelectrodes with greatly enhanced photoelectrochemical activity, International Journal of Hydrogen Energy 43(4) (2018) 2057-2063.
[18] Z. Miao, G. Wang, L. Li, C. Wang, X. Zhang, Fabrication of black TiO 2/TiO 2 homojunction for enhanced photocatalytic degradation, Journal of Materials Science 54(23) (2019) 14320-14329.
[19] F. Rasouli, A. Rouhollahi, F. Ghahramanifard, Gradient doping of copper in ZnO nanorod photoanode by electrodeposition for enhanced charge separation in photoelectrochemical water splitting, Superlattices and Microstructures 125 (2019) 177-189.
[20] J. Lynch, C. Giannini, J.K. Cooper, A. Loiudice, I.D. Sharp, R. Buonsanti, Substitutional or Interstitial Site-Selective Nitrogen Doping in TiO2 Nanostructures, The Journal of Physical Chemistry C 119(13) (2015) 7443-7452.
[21] Z. Liu, Y. Li, C. Liu, J. Ya, L. E, W. Zhao, D. Zhao, L. An, TiO2 photoanode structure with gradations in V concentration for dye-sensitized solar cells, ACS applied materials & interfaces 3(5) (2011) 1721-1725.
[22] N. Delegan, R. Daghrir, P. Drogui, M.A. El Khakani, Bandgap tailoring of in-situ nitrogen-doped TiO2 sputtered films intended for electrophotocatalytic applications under solar light, Journal of Applied Physics 116(15) (2014) 153510.
[23] B.R. Bricchi, M. Ghidelli, L. Mascaretti, A. Zapelli, V. Russo, C.S. Casari, G. Terraneo, I. Alessandri, C. Ducati, A.L. Bassi, Integration of plasmonic Au nanoparticles in TiO2 hierarchical structures in a single-step pulsed laser co-deposition, Materials & Design 156 (2018) 311-319.
[24] Y. Suda, H. Kawasaki, T. Ueda, T. Ohshima, Preparation of high quality nitrogen doped TiO2 thin film as a photocatalyst using a pulsed laser deposition method, Thin solid films 453 (2004) 162-166.
[25] S. Murcia-López, C. Fàbrega, D. Monllor-Satoca, M.D. Hernández-Alonso, G.n. Penelas-Pérez, A. Morata, J.R. Morante, T. Andreu, Tailoring multilayered BiVO4 photoanodes by pulsed laser deposition for water splitting, ACS applied materials & interfaces 8(6) (2016) 4076-4085.
[26] R.P. Antony, M. Zhang, K. Zhou, S.C.J. Loo, J. Barber, L.H. Wong, Synergistic effect of porosity and gradient doping in efficient solar water oxidation of catalyst-free gradient Mo: BiVO4, ACS omega 3(3) (2018) 2724-2734.
[27] K. Drogowska, Z. Tarnawski, A. Brudnik, E. Kusior, M. Sokołowski, K. Zakrzewska, A. Reszka, N.-T. Kim-Ngan, A. Balogh, RBS, XRR and optical reflectivity measurements of Ti–TiO2 thin films deposited by magnetron sputtering, Materials Research Bulletin 47(2) (2012) 296-301.
[28] A. Mirzaei, L. Yerushalmi, Z. Chen, F. Haghighat, J. Guo, Enhanced photocatalytic degradation of sulfamethoxazole by zinc oxide photocatalyst in the presence of fluoride ions: Optimization of parameters and toxicological evaluation, Water Research 132 (2018) 241-251.

[29] J. Zhang, Z. Wang, M. Fan, P. Tong, J. Sun, S. Dong, J. Sun, Ultra-light and compressible 3D BiOCl/RGO aerogel with enriched synergistic effect of adsorption and photocatalytic degradation of oxytetracycline, Journal of Materials Research and Technology 8(5) (2019) 4577-4587.
[30] C.M. Courtney, S.M. Goodman, J.A. McDaniel, N.E. Madinger, A. Chatterjee, P. Nagpal, Photoexcited quantum dots for killing multidrug-resistant bacteria, Nature materials 15(5) (2016) 529-534.
[31] M. Nawaz, W. Miran, J. Jang, D.S. Lee, Stabilization of Pickering emulsion with surface-modified titanium dioxide for enhanced photocatalytic degradation of Direct Red 80, Catalysis Today 282 (2017) 38-47.
[32] M. Xing, J. Zhang, F. Chen, New approaches to prepare nitrogen-doped TiO2 photocatalysts and study on their photocatalytic activities in visible light, Applied Catalysis B: Environmental 89(3) (2009) 563-569.
[33] R. Asahi, T. Morikawa, T. Ohwaki, K. Aoki, Y. Taga, Visible-light photocatalysis in nitrogen-doped titanium oxides, science 293(5528) (2001) 269-271.
[34] T. Morikawa, R. Asahi, T. Ohwaki, K. Aoki, Y. Taga, Band-gap narrowing of titanium dioxide by nitrogen doping, Japanese Journal of Applied Physics 40(6A) (2001) L561.
[35] S. Hoang, S. Guo, N.T. Hahn, A.J. Bard, C.B. Mullins, Visible light driven photoelectrochemical water oxidation on nitrogen-modified TiO2 nanowires, Nano letters 12(1) (2012) 26-32.
[36] S.S. Lee, H. Bai, Z. Liu, D.D. Sun, Optimization and an insightful properties—Activity study of electrospun TiO2/CuO composite nanofibers for efficient photocatalytic H2 generation, Applied Catalysis B: Environmental 140-141 (2013) 68-81.
[37] H. Matsui, H. Tabata, N. Hasuike, H. Harima, B. Mizobuchi, Epitaxial growth and characteristics of N-doped anatase TiO 2 films grown using a free-radical nitrogen oxide source, Journal of applied physics 97(12) (2005) 123511.
[38] K. Ozawa, M. Emori, S. Yamamoto, R. Yukawa, S. Yamamoto, R. Hobara, K. Fujikawa, H. Sakama, I. Matsuda, Electron–Hole Recombination Time at TiO2 Single-Crystal Surfaces: Influence of Surface Band Bending, The Journal of Physical Chemistry Letters 5(11) (2014) 1953-1957.
[39] M. Baker, H. Fakhouri, R. Grilli, J. Pulpytel, W. Smith, F. Arefi-Khonsari, Effect of total gas pressure and O2/N2 flow rate on the nanostructure of N-doped TiO2 thin films deposited by reactive sputtering, Thin Solid Films 552 (2014) 10-17.
[40] L. Zeng, W. Song, M. Li, X. Jie, D. Zeng, C. Xie, Comparative study on the visible light driven photocatalytic activity between substitutional nitrogen doped and interstitial nitrogen doped TiO2, Applied Catalysis A: General 488 (2014) 239-247.
[41] T. He, X. Zeng, S. Rong, The controllable synthesis of substitutional and interstitial nitrogen-doped manganese dioxide: the effects of doping sites on enhancing the catalytic activity, Journal of Materials Chemistry A 8(17) (2020) 8383-8396.
[42] R. Ghosh, Y. Hara, L. Alibabaei, K. Hanson, S. Rangan, R. Bartynski, T.J. Meyer, R. Lopez, Increasing photocurrents in dye sensitized solar cells with tantalum-doped titanium oxide photoanodes obtained by laser ablation, ACS applied materials & interfaces 4(9) (2012) 4566-4570.
[43] J.H. Noh, J.H. Park, H.S. Han, D.H. Kim, B.S. Han, S. Lee, J.Y. Kim, H.S. Jung, K.S. Hong, Aligned photoelectrodes with large surface area prepared by pulsed laser deposition, The Journal of Physical Chemistry C 116(14) (2012) 8102-8110.
[44] F. Di Fonzo, C.S. Casari, V. Russo, M.F. Brunella, A.L. Bassi, C.E. Bottani, Hierarchically organized nanostructured TiO2 for photocatalysis applications, Nanotechnology 20(1) (2008) 015604.
[45] F. Sauvage, F. Di Fonzo, A. Li Bassi, C.S. Casari, V. Russo, G. Divitini, C. Ducati, C.E. Bottani, P. Comte, M. Graetzel, Hierarchical TiO2 photoanode for dye-sensitized solar cells, Nano letters 10(7) (2010) 2562-2567.
[46] Y. Li, Z.Y. Fu, B.L. Su, Hierarchically structured porous materials for energy conversion and storage, Advanced Functional Materials 22(22) (2012) 4634-4667.

[47] S.H. Kang, S.H. Choi, M.S. Kang, J.Y. Kim, H.S. Kim, T. Hyeon, Y.E. Sung, Nanorod-based dye-sensitized solar cells with improved charge collection efficiency, Advanced Materials 20(1) (2008) 54-58.
[48] H. Dotan, K. Sivula, M. Grätzel, A. Rothschild, S.C. Warren, Probing the photoelectrochemical properties of hematite (α-Fe 2 O 3) electrodes using hydrogen peroxide as a hole scavenger, Energy & Environmental Science 4(3) (2011) 958-964.
[49] N. Denisov, J. Yoo, P. Schmuki, Effect of different hole scavengers on the photoelectrochemical properties and photocatalytic hydrogen evolution performance of pristine and Pt-decorated TiO2 nanotubes, Electrochimica Acta 319 (2019) 61-71.
[50] Z. Luo, C. Li, S. Liu, T. Wang, J. Gong, Gradient doping of phosphorus in Fe 2 O 3 nanoarray photoanodes for enhanced charge separation, Chemical science 8(1) (2017) 91-100.
[51] X. Cheng, Q. Cheng, X. Deng, P. Wang, H. Liu, A facile and novel strategy to synthesize reduced TiO2 nanotubes photoelectrode for photoelectrocatalytic degradation of diclofenac, Chemosphere 144 (2016) 888-894.
[52] R. Daghrir, P. Drogui, A. Dimboukou-Mpira, M.A. El Khakani, Photoelectrocatalytic degradation of carbamazepine using Ti/TiO2 nanostructured electrodes deposited by means of a pulsed laser deposition process, Chemosphere 93(11) (2013) 2756-2766.
[53] A.S. Mestre, A.P. Carvalho, Photocatalytic Degradation of Pharmaceuticals Carbamazepine, Diclofenac, and Sulfamethoxazole by Semiconductor and Carbon Materials: A Review, Molecules 24(20) (2019) 3702.
[54] E.L. Schymanski, H.P. Singer, J. Slobodnik, I.M. Ipolyi, P. Oswald, M. Krauss, T. Schulze, P. Haglund, T. Letzel, S. Grosse, Non-target screening with high-resolution mass spectrometry: critical review using a collaborative trial on water analysis, Analytical and bioanalytical chemistry 407(21) (2015) 6237-6255.
[55] K. Hiller, B. Masloch, M. Goebl, K. Asmus, Mechanism of the hydroxyl radical induced oxidation of methionine in aqueous solution, Journal of the American Chemical Society 103(10) (1981) 2734-2743.
[56] S. Wang, J. Wang, Comparative study on sulfamethoxazole degradation by Fenton and Fe (II)-activated persulfate process, Rsc Advances 7(77) (2017) 48670-48677.
[57] J. Du, W. Guo, H. Wang, R. Yin, H. Zheng, X. Feng, D. Che, N. Ren, Hydroxyl radical dominated degradation of aquatic sulfamethoxazole by Fe0/bisulfite/O2: Kinetics, mechanisms, and pathways, Water research 138 (2018) 323-332.
[58] S.K. Ray, D. Dhakal, S.W. Lee, Insight into sulfamethoxazole degradation, mechanism, and pathways by AgBr-BaMoO4 composite photocatalyst, Journal of Photochemistry and Photobiology A: Chemistry 364 (2018) 686-695.
[59] T. Su, H. Deng, J.P. Benskin, M. Radke, Biodegradation of sulfamethoxazole photo-transformation products in a water/sediment test, Chemosphere 148 (2016) 518-525.
[60] L. Geis-Asteggiante, A. Nuñez, S.J. Lehotay, A.R. Lightfield, Structural characterization of product ions by electrospray ionization and quadrupole time-of-flight mass spectrometry to support regulatory analysis of veterinary drug residues in foods, Rapid Communications in Mass Spectrometry 28(10) (2014) 1061-1081.
[61] M. Długosz, P. Żmudzki, A. Kwiecień, K. Szczubiałka, J. Krzek, M. Nowakowska, Photocatalytic degradation of sulfamethoxazole in aqueous solution using a floating TiO2-expanded perlite photocatalyst, Journal of Hazardous Materials 298 (2015) 146-153.
[62] C. Qi, X. Liu, C. Lin, X. Zhang, J. Ma, H. Tan, W. Ye, Degradation of sulfamethoxazole by microwave-activated persulfate: Kinetics, mechanism and acute toxicity, Chemical Engineering Journal 249 (2014) 6-14.
[63] M. Gmurek, H. Horn, M. Majewsky, Phototransformation of sulfamethoxazole under simulated sunlight: Transformation products and their antibacterial activity toward Vibrio fischeri, Science of The Total Environment 538 (2015) 58-63.

[64] X. Zhao, J. Qu, H. Liu, Z. Qiang, R. Liu, C. Hu, Photoelectrochemical degradation of anti-inflammatory pharmaceuticals at Bi2MoO6–boron-doped diamond hybrid electrode under visible light irradiation, Applied Catalysis B: Environmental 91(1) (2009) 539-545.
[65] R. Daghrir, P. Drogui, N. Delegan, M.A. El Khakani, Removal of chlortetracycline from spiked municipal wastewater using a photoelectrocatalytic process operated under sunlight irradiations, Science of The Total Environment 466 (2014) 300-305.
[66] S.-S. Liu, Q.-J. Xing, Y. Chen, M. Zhu, X.-H. Jiang, S.-H. Wu, W. Dai, J.-P. Zou, Photoelectrochemical Degradation of Organic Pollutants Using BiOBr Anode Coupled with Simultaneous CO2 Reduction to Liquid Fuels via CuO Cathode, ACS Sustainable Chemistry & Engineering 7(1) (2018) 1250-1259.
[67] X. Cheng, H. Liu, Q. Chen, J. Li, P. Wang, Enhanced photoelectrocatalytic performance for degradation of diclofenac and mechanism with TiO2 nano-particles decorated TiO2 nano-tubes arrays photoelectrode, Electrochimica Acta 108 (2013) 203-210.
[68] Z. Hua, Z. Dai, X. Bai, Z. Ye, P. Wang, H. Gu, X. Huang, Copper nanoparticles sensitized TiO2 nanotube arrays electrode with enhanced photoelectrocatalytic activity for diclofenac degradation, Chemical Engineering Journal 283 (2016) 514-523.
[69] M. Zhang, X. Li, Q. Zhao, S. Fan, Z. Jiang, G. Chen, AgInS2 nanoparticles modified TiO2 nanotube array electrodes: Ultrasonic-assisted SILAR preparation and mechanism of enhanced photoelectrocatalytic activity, Molecular Catalysis 442 (2017) 97-106.